Site-resolved oxygen *K*-edge ELNES of the layered double perovskite La_2CuSnO_6

M. Haruta, H. Kurata, H. Komatsu, Y. Shimakawa, and S. Isoda
Institute for Chemical Research, Kyoto University, Uji, Kyoto 611-0011, Japan
(Received 14 July 2009; revised manuscript received 17 September 2009; published 21 October 2009)

Electron energy-loss spectroscopy (EELS) combined with scanning transmission electron microscopy (STEM) allows for the investigation of the local electronic structure with atomic column resolution, owing to the development of spherical aberration correctors. In the present research, we report *B*-site-resolved oxygen *K*-edge energy-loss near-edge structure (ELNES) measured from a double perovskite La_2CuSnO_6 (LCSO) using STEM-EELS. There are two kinds of BO_6 (B=Sn and Cu) octahedrons, arranged in layers in the LCSO crystal. The observed site-resolved oxygen *K*-edge ELNES showed different features reflecting local chemical bonding around the Sn and Cu ions. In particular, it is demonstrated that the local electronic structure in the distorted CuO_6 octahedron caused by the Jahn-Teller effect can be detected by site-resolved ELNES.

DOI: 10.1103/PhysRevB.80.165123 PACS number(s): 82.80.Pv, 31.15.ae, 68.37.Ma, 79.20.Uv

I. INTRODUCTION

With recent developments in correcting electron optical aberrations, it is now possible to analyze structural images with subangstrom resolution.[1–4] Electron energy-loss spectroscopy (EELS) combined with scanning transmission electron microscopy (STEM) has realized single atomic column analysis[5–10] and element-selective imaging with atomic resolution.[11–13] As a next step, detailed chemical bond mapping at atomic resolutions is anticipated in the near future. Site-resolved electron energy-loss near-edge structure (ELNES) is thus very important to realize chemical bond mapping.[14,15]

Perovskite-structured oxides have the general formula ABO_3, which can be described as a framework of corner-shared BO_6 octahedrons with 12-coordinated *A* cations. When two different cations are introduced at the *B* site, double perovskite structures with the formula $A_2BB'O_6$ are formed. Depending on differences in size and charge of the *B*-site cations, three types of structural arrangements of cations are known: random, rocksalt, and layered.[16] In the majority of ordered double perovskite oxides ($A_2BB'O_6$), *B* and *B'* sites have the rocksalt structure, whereas only Cu^{2+} and Sn^{4+} ions in La_2CuSnO_6 (LCSO) are arranged in layers at ambient pressures.[17,18] The layered crystal structure determined by powder x-ray diffraction analysis is shown schematically in Fig. 1. The La column–La column distance around the Cu ion is shorter than around the Sn ion because the CuO_6 octahedrons are slightly distorted by the Jahn-Teller effect. The alternation of CuO_6 and SnO_6 octahedral layers and buckling of CuO_2 and SnO_2 sheets induce a monoclinic superstructure with the following lattice parameters: a=0.8510, b=0.7815, c=0.7817 nm, and β=91.151°, corresponding almost to $2a_p \times 2a_p \times 2a_p$ (a_p is the lattice parameter for a cubic perovskite). LCSO had been expected to show superconductivity by appropriate carrier doping of Sr^{2+} or Ca^{2+} substitution for La^{3+}. However, all attempts had tried unsuccessfully to find superconductivity because of heavily buckled Cu-O-Cu bonds in the CuO_2 sheets.[19,20] There are eight nonequivalent oxygen atoms (two O1, four O2, two O3, four O4, four O5, two O6, four O7, and two O8 atoms) with different atomic coordinates in one unit cell. By taking advantage of the electron channeling effect, it should be possible to excite specific oxygen atoms coordinating to a *B* cation in the unit cell when the electron probe is placed at the *B*-site atom. The layered structure such as LCSO is suitable for examining the site-resolved EELS. In the present research, we demonstrate the *B*-site-resolved oxygen *K*-ELNES measured from LCSO using the STEM-EELS method, which can be used to extract the local electronic structure arising from the Jahn-Teller distortion of the CuO_6 octahedron. Recently, Varela *et al.* also reported the noticeable change in the prepeak of O *K*-edge ELNES calculated for the nonequivalent O sites in a Jahn-Teller distorted MnO_6 of manganite perovskites.[21] Since the Jahn-Teller effect is important for the high-temperature cuprate superconductor, it should be valuable to examine this effect at high spatial resolution using the STEM-EELS method.

II. METHODOLOGY

The sample with a layered double perovskite LCSO film was fabricated using a pulsed laser deposition technique.[22]

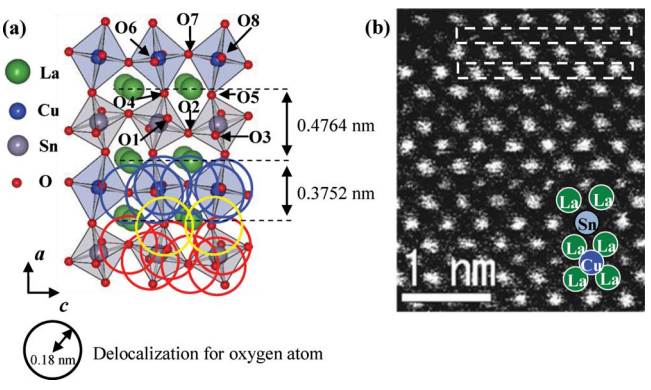

FIG. 1. (Color online) (a) Structure of layered La_2CuSnO_6 analyzed by x-ray diffraction. There are eight nonequivalent oxygen atoms in the unit cell. The circles (radius of 0.18 nm) indicate delocalization of inelastic scattering by the excitation of O 1*s* electrons. Blue, red, and yellow circles show the O sites binding only to Cu, only to Sn, and linking to both Cu and Sn, respectively. (b) Atomic resolution HAADF image of LCSO. The scanning areas for site-resolved EELS spectra are illustrated as rectangular areas enclosed by the white dashed lines.

LCSO thin films were grown heteroepitaxially on $SrTiO_3$ substrates. The growth temperature was 670 °C in an oxygen partial pressure of 0.1 Torr, which are optimized conditions for fabricating the layered structure. Cross-sectional samples were thinned down to electron transparency by ion milling. The thickness of the observed area is about 30 nm, as estimated by EELS measurements. Atomic resolution STEM imaging and EELS measurements were performed at room temperature using a 200 kV TEM/STEM (JEM-9980TKP1; C_s=−0.025 mm, C_5=15 mm) equipped with a spherical aberration corrector for the illuminating lens system. This provided an incident electron probe of less than 0.1 nm in diameter with a convergent semiangle of approximately 23 mrad. Atomic resolution high-angle annular dark field (HAADF) images were obtained with a detection semiangle of 70–170 mrad. EELS spectra were obtained using an omega filter with a collection semiangle of 10 mrad. The energy resolution measured by the full width at half maximum of a zero-loss peak was about 0.5 eV using a cold field emission gun.

First-principles band structure calculations were performed by a full-potential linear augmented plane wave plus local orbital method using the WIEN2K code.[23] ELNES spectra were calculated using the TELNES.2 package incorporated in the WIEN2K code.[24] The effect of a core hole was taken into account in the calculations by introducing a hole in the oxygen 1*s* state at each nonequivalent oxygen site and adding an electron in the valence band. Since the unit cell of the LCSO is relatively large, as mentioned previously, calculation including a core hole was carried out by using the primitive unit cell for execution within a practical time period.

In order to evaluate the spatial resolution of site-resolved EELS, it is worth estimating the delocalization of inelastic scattering due to excitation of the oxygen 1*s* electron. The delocalization, d_E, of the inelastic electrons losing an energy of ΔE can be simply represented by the following equation:[25,26]

$$d_E = \frac{\lambda}{2}\left(\frac{2E}{\Delta E}\right)^{3/4} = \frac{\lambda}{2\theta_E^{3/4}}. \quad (1)$$

Here, λ and E are the wavelength and beam energy of the incident electrons, respectively, and $\theta_E = \Delta E/(2E)$ is a characteristic inelastic scattering angle. The delocalization of oxygen *K*-edge spectra (ΔE=532 eV) excited by a beam energy of 200 keV is estimated to be 0.18 nm, which indicates that the delocalization is sufficiently narrow to discriminate contributions from oxygen atoms in each layer of the LCSO, as shown with circles in Fig. 1(a). Therefore, it can be expected that specific oxygen atoms coordinating to a *B*-site cation in the unit cell are separately excited when the electron probe is placed on the *B*-site cation. Figure 1(b) shows a typical atomic resolution HAADF image of LCSO, wherein *B*-site cations can be clearly distinguished owing to *Z*-contrast imaging.[27] In order to avoid electron damage to the specimen, O *K*-edge ELNES spectra were acquired by scanning the electron probe on equivalent *B*-site columns along the *c* axis, as illustrated by the rectangular areas enclosed by white dotted lines in Fig. 1(b). Another factor affecting the spatial resolution of the site-resolved EELS spectra is the propagation of the incident electron probe in the crystal, the so-called electron channeling.[28] The dynamical behavior of electrons in the crystal can be calculated by the multislice method.[29] Figure 2 shows two-dimensional maps of the electron wave function as a function of the specimen thickness calculated by the WIN HREM Version 3.5 software when the incident electron beam is placed on the *B*-site columns and the middle point of the Cu-Cu columns or Sn-Sn columns, indicated by the arrows at the top row in the figure. When the electron probe is positioned on the *B*-site columns [Figs. 2(a) and 2(c)], most of the electrons propagate though the *B* site and its nearest-neighbor O columns. Even when the electrons disperse with increasing specimen thickness, most effectively dechannel to the nearest-neighbor oxygen atoms forming each BO_6 octahedron. When the incident electron probe is located on the middle point of Cu and Cu [Fig. 2(b)] or Sn and Sn [Fig. 2(d)], very close to the oxygen atom shared with the same *B* cations, most of the electrons effectively propagate near the oxygen atom, although it appears that a small amount of electrons dechannel to La sites. Therefore, from the viewpoint of the electron channeling process, it can be expected that specific oxygen atoms coordinating to each *B*-site cation in the unit cell are separately excited when the electron probe is scanned on the same *B*-site cation.

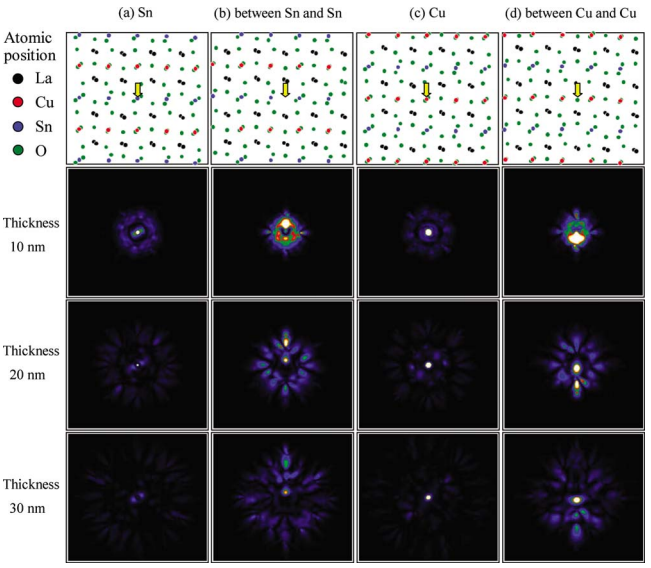

FIG. 2. (Color online) Two-dimensional map of the electron wave function as a function of sample thickness when the electron probe was positioned on (a) a Sn column, (b) the middle of Sn and Sn, (c) the Cu column, and (d) the middle of Cu and Cu. The position of electron probe is indicated by a yellow arrow in the projected atomic map images.

III. RESULTS AND DISCUSSION

Figure 3 shows three O *K*-edge ELNES spectra acquired by scanning an electron probe over a whole unit cell of LCSO, only from the Sn or the Cu site. These spectra clearly have different shapes; the peak labeled A is clearly observed

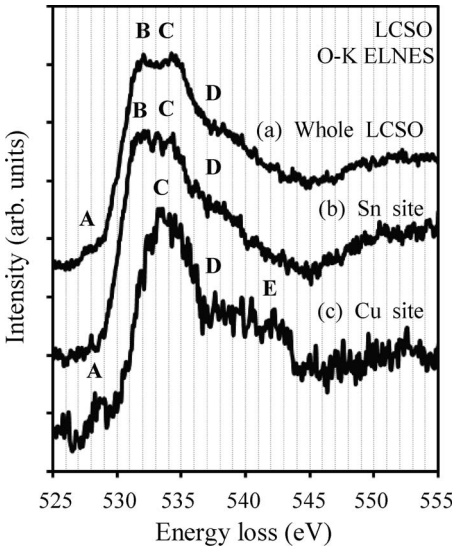

FIG. 3. Experimental O *K*-edge ELNES from (a) the whole unit cell of LCSO, (b) Sn site, and (c) Cu site.

in the spectrum from the Cu site, and the main peak consists of two peaks labeled B and C as observed in the spectra from the whole unit cell and the Sn site, while the spectrum from the Cu site only shows peak C. These characteristic features suggest that the chemically different oxygen atoms contribute individually to the spectra of the Sn and Cu sites, although the spectrum from the whole unit cell contains the excitation of all oxygen sites. As mentioned in Sec. I, there are eight nonequivalent oxygen sites in the unit cell, which should contribute to the O *K*-edge ELNES differently. Therefore, for simulating the ELNES spectrum, it is necessary to calculate the partial density of states (PDOS) at each individual oxygen site.

Figure 4 shows the O *K*-edge ELNES calculated for each individual oxygen site (from O1 to O8) in the LCSO. Here, we show the spectra calculated by including a core hole in the 1*s* state of each oxygen atom (solid lines) together with those from ground state calculations (broken lines) without a core hole. The core-hole effect appears differently in each

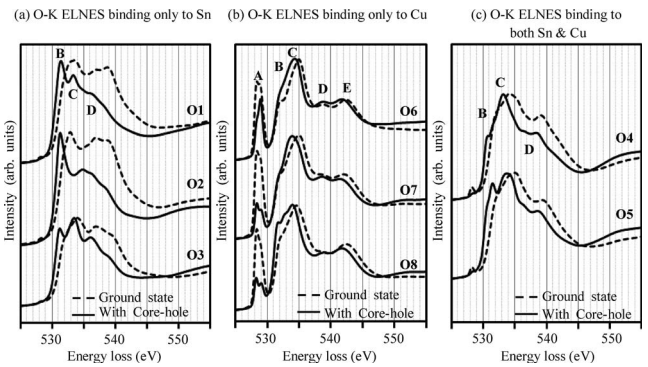

FIG. 4. Calculated O *K*-edge ELNES for individual oxygen sites in LCSO. O *K* ELNES of O sites (a) binding only to a Sn atom, (b) binding only to a Cu atom, and (c) binding to both Sn and Cu atoms. Solid lines are spectra calculated by including the core-hole effect and the dotted line by the ground state.

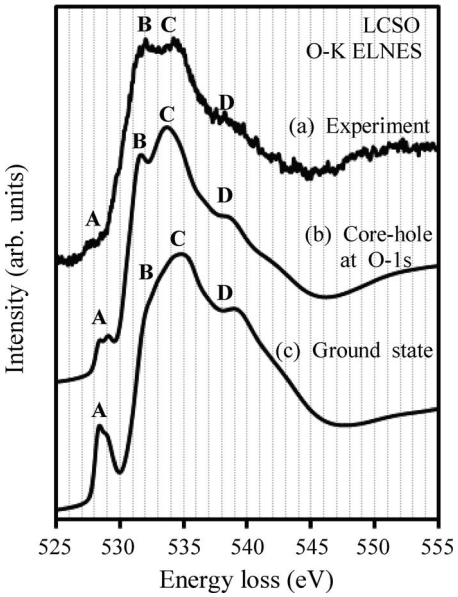

FIG. 5. O *K*-edge ELNES of LCSO obtained from the whole unit cell. (a) Experimental results, (b) calculated with the O 1*s* core-hole state, and (c) calculated for the ground state. The calculated spectra were summed with a weight considering the number of sites contained in the unit cell.

spectrum, which will be discussed later. These spectra can be classified into three groups in relation to the nearest-neighbor *B*-site atoms: the spectra of oxygen atoms binding only to a Sn atom [Fig. 4(a)] or only to a Cu atom [Fig. 4(b)] and the spectra of oxygen atoms linking both Sn and Cu atoms [Fig. 4(c)]. In order to simulate the O *K*-edge ELNES acquired over the whole unit cell, all the calculated spectra are summed up by taking into account the occupancy of each atomic site. Figures 5(b) and 5(c) show the calculated spectra compared with the experimental spectrum [Fig. 5(a)] acquired from the whole unit cell. The calculated spectrum including a core hole is in better agreement with the experimental one. By comparing the spectral features with the PDOS, we find that peak A can be attributed to the transition to the O 2*p* states hybridized with Cu 3*d* states near the Fermi level, while peaks B–D correspond mainly to the transitions to the O 2*p* states hybridized with Sn 5*s*, La 5*d* and Cu 4*s*, and Sn 5*p* and/or Cu 4*s* states, respectively. Although this spectrum includes the contribution from all O sites, site-resolved spectra can discriminate individual contributions.

Figure 6 shows a comparison between the site-resolved spectra acquired experimentally from the Sn and Cu sites and the corresponding calculated spectra including the core-hole effect. Since the value of the spatial resolution of the present EELS experiment is not very obvious because of delocalization of inelastic scattering [Fig. 1(a)] and beam dechanneling (Fig. 2), two types of calculated spectra are shown in Fig. 6. One is constructed with all oxygen atoms forming the SnO_6 and CuO_6 octahedrons (a-2 and b-2), while the other eliminates the contribution from the apex sites (O4 and O5) of the octahedrons (a-3 and b-3). The experimental spectra (a-1 and b-1 in Fig. 6) acquired from the Sn and Cu sites agree well with the calculated spectra (a-2 and b-2 in Figs. 6) including

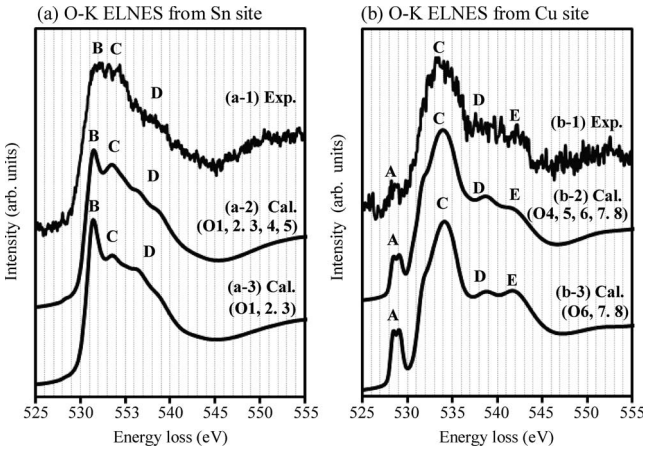

FIG. 6. Site-resolved spectra from the (a) Sn site and (b) Cu site, where spectrum 1 is the experimental spectrum, the calculated spectrum 2 includes the contribution from all O sites surrounding each *B*-site cation, and the calculated spectrum 3 eliminates the contribution from the apex O sites in octahedrons.

the contribution from all oxygen atoms forming the SnO_6 or CuO_6 octahedrons, respectively. The clear difference in the O *K*-edge ELNES indicates that the experimental site-resolved spectra contain the local electronic structure around the Sn or Cu separately, although the linking oxygen atoms (O4 and O5) contribute to both experimental site-resolved spectra. The reason why O4 and O5 sites contribute to both the spectra from Cu-O and Sn-O layers is attributed to the delocalization of the inelastic scattering as discussed in Ref. 21. The site-resolved O *K*-edge ELNES shows the following specific features. Peak A due to transitions to the hybridized O 2*p*-Cu 3*d* states appears only in the CuO_6 spectrum [Fig. 6(b)], while peak B attributed to the transition to the O 2*p* states hybridized with Sn 5*s* states appears predominantly in the SnO_6 spectrum [Fig. 6(a)]. Peaks C and D appear in both spectra because these peaks mainly originate from transitions to the hybridized O 2*p*-La 5*d* states and O 2*p*-Sn 5*p* and/or Cu 4*s* states, respectively.

It should be emphasized that prepeak A attributed to the transition to the O 2*p* state hybridized with the Cu 3*d* state is not observed in the SnO_6 spectrum, although oxygen atoms (O4 and O5) linking Sn and Cu also contribute to this spectrum. This means that there are no unoccupied O 2*p* states hybridized with the Cu 3*d* state in the local DOS at O4 and O5 sites. This result contains important information on local electronic structure arising from the Jahn-Teller distortion of the CuO_6 octahedrons. Figure 7 shows the structures of CuO_6 and SnO_6 octahedrons in the LCSO as determined by x-ray diffraction analysis.[17] The CuO_6 octahedron in the LCSO is elongated in the *z* direction by the Jahn-Teller effect. Such a distortion from cubic symmetry (O_h) leads to a splitting of the t_{2g} and e_g states, as illustrated in Fig. 7. The crystal field of the Cu 3*d* states in the distorted CuO_6 octahedron splits the t_{2g} states into $b_{2g}(d_{xy})$ and $e_g(d_{yz},d_{zx})$ states and the e_g states into $b_{1g}(d_{x^2-y^2})$ and $a_{1g}(d_{3z^2-r^2})$ states.[30] Since the $b_{2g}(d_{xy})$ and $e_g(d_{yz},d_{zx})$ states are occupied with $Cu^{2+}(d^9)$ ion, there are two possibilities for the electron configuration at the top of the Cu 3*d* states: $(b_{1g})^2(a_{1g})^1$ or

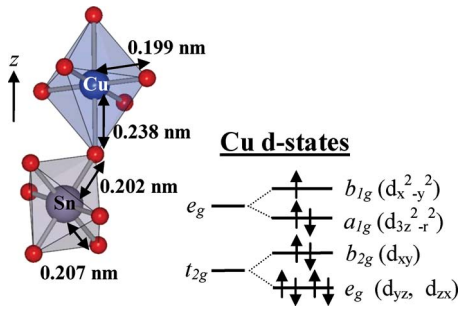

FIG. 7. (Color online) (a) Local structure of CuO_6 and SnO_6 octahedrons in the LCSO crystal. The CuO_6 octahedron is distorted by the Jahn-Teller effect. The bond lengths shown in the CuO_6 and SnO_6 octahedrons are average values. (b) Crystal-field splitting of Cu 3*d* states owing to the Jahn-Teller distortion.

$(a_{1g})^2(b_{1g})^1$. The $b_{1g}(d_{x^2-y^2})$ state is extended into the in plane, while the $a_{1g}(d_{3z^2-r^2})$ state is directed in the *z* direction forming hybridized states at the O4 and O5 sites. This experimental result clearly indicates that the Cu 3*d* hole should be in the $b_{1g}(d_{x^2-y^2})$ state because there are no 3*d* holes at the O4 and O5 sites linking both the Sn and Cu atoms, as previously mentioned. Therefore, it is concluded that the electron configuration should be $(a_{1g})^2(b_{1g})^1$ in the ground state. Such a configuration suggests that electrostatic repulsion between Cu and O atoms at the O4 and O5 sites is stronger than that for in-plane O atoms, which results in a slight expansion of bond lengths between the Cu and the apex O sites (O4 and O5 atoms) compared to those of the in-plane O atoms. The elongated distortion along the *z* direction is consistent with the structural analysis results, shown in Fig. 7. Consequently, it is demonstrated that the Jahn-Teller effect can be detected by site-resolved EELS.

Finally, we discuss core-hole effects in the material, which operate differently at the eight nonequivalent oxygen sites, as shown in Fig. 4. The core-hole potential generally modifies the distribution of DOS in the bottom of the unoccupied band,[31–33] leading to a change in ELNES. In the case of oxygen atoms around the Sn site, the spectrum shifts down as a whole to the Fermi level due to the core-hole effect. Peak B corresponding to the transition to the hybridized O 2*p*-Sn 5*s* states is enhanced, while the intensity of peak D is considerably reduced due to transitions to the O 2*p* states hybridized with Sn 5*p* states. Such a spectral modification is typically obtained as an excitonic effect in ionic insulators;[34] therefore, it appears that the character of chemical bonding in the SnO_6 octahedron is locally an ionic one. On the other hand, in the case of oxygen atoms around a Cu site, the intensity of peak A due to the transition to the O 2*p* states hybridized with the Cu 3*d* states is significantly weakened by the core-hole effect, whereas the other peaks at higher energy are almost unchanged. A similar decrease in the prepeak intensity owing to the core-hole effect has been reported for O *K*-edge excitation spectra obtained from CuO (Ref. 35) and $LaCoO_3$.[36] This decrease in the prepeak intensity might indicate that some empty O 2*p* states lying at the bottom of the conduction band could be pulled below the Fermi level to effectively screen the core-hole potential[37] because the bottom of the conduction band is mainly com-

posed of Cu 3*d* states which are near the Fermi level compared to the Sn 5*sp* states.

IV. CONCLUSIONS

In the present research, *B*-site-resolved oxygen *K*-edge ELNES was measured from LCSO using the STEM-EELS method. The experimental site-resolved spectra clearly have different shapes reflecting the local electronic structure around the SnO_6 and CuO_6 octahedrons. The prepeak attributed to the transition to O 2*p* states hybridized with Cu 3*d* states was not observed in the spectrum acquired from oxygen atoms around the Sn site, although oxygen atoms (O4 and O5) linking Sn and Cu contribute to this spectrum, indicating that there are no unoccupied O 2*p* states hybridized with Cu 3*d* states at the O4 and O5 sites. From this result, the electron configuration at the top of the Cu 3*d* state was determined to be $(a_{1g})^2(b_{1g})^1$ caused by the Jahn-Teller distortion of the CuO_6 octahedrons. Consequently, it was demonstrated that the Jahn-Teller effect was detected only in the CuO_6 octahedrons by site-resolved EELS.

The experimental spectra agree well with the calculated spectra including the core-hole effect. The core-hole effects on any oxygen *K*-edge spectra have a tendency to shift the excitation energy a little lower. It was also found that the core-hole effect appears differently around Sn and Cu sites, as shown in Fig. 4. In the case of O around the Sn site, the O 2*p* states hybridized with the Sn 5*s* states are enhanced by the core-hole effect. On the other hand, in the case of O around the Cu site, O 2*p* states hybridized with the Cu 3*d* states are weakened by the core-hole effect.

ACKNOWLEDGMENTS

This work was partly supported by Grants-in-Aid for Scientific Research Grants No. 19GS0207 and No. 19310071 and also by JSPS Fellows Grant No. 20-145 from the Ministry of Education, Culture, Sports, Science and Technology, Japan. We acknowledge Kawasaki, Otsuka, and Nishimura of TRC for preparing the cross-section samples.

[1] P. E. Batson, N. Dellby, and O. L. Krivanek, Nature (London) **418**, 617 (2002).
[2] P. D. Nellist, M. F. Chisholm, N. Dellby, O. L. Krivanek, M. F. Murfitt, Z. S. Szilagyi, A. R. Lupini, A. Borisevich, W. H. Sides, Jr., and S. J. Pennycook, Science **305**, 1741 (2004).
[3] H. Sawada, F. Hosokawa, T. Kaneyama, T. Ishizawa, M. Terao, M. Kawazoe, T. Sannomiya, T. Tomita, Y. Kondo, T. Tanaka, Y. Oshima, Y. Tanishiro, N. Yamamoto, and K. Takayanagi, Jpn. J. Appl. Phys., Part 2 **46**, L568 (2007).
[4] C. Kisielowski, B. Freitag, M. Bischoff, H. van Lin, S. Lazar, G. Knippels, P. Tiemeijer, M. van der Stam, S. von Harrach, M. Stekelenburg, M. Haider, S. Uhlemann, H. Müller, P. Hartel, B. Kabius, D. Miller, I. Petrov, E. A. Olson, T. Donchev, E. A. Kenik, A. R. Lupini, J. Bentley, S. J. Pennycook, I. M. Anderson, A. M. Minor, A. K. Schmid, T. Duden, V. Radmilovic, Q. M. Ramasse, M. Watanabe, R. Erni, E. A. Stach, P. Denes, and U. Dahmen, Microsc. Microanal. **14**, 469 (2008).
[5] N. D. Browning, M. F. Chisholm, and S. J. Pennycook, Nature (London) **366**, 143 (1993).
[6] P. E. Batson, Nature (London) **366**, 727 (1993).
[7] D. A. Muller, T. Sorsch, S. Moccio, F. H. Baumann, K. Evans-Lutterodt, and G. Timp, Nature (London) **399**, 758 (1999).
[8] M. Varela, S. D. Findlay, A. R. Lupini, H. M. Christen, A. Y. Borisevich, N. Dellby, O. L. Krivanek, P. D. Nellist, M. P. Oxley, L. J. Allen, and S. J. Pennycook, Phys. Rev. Lett. **92**, 095502 (2004).
[9] A. Ziegler, J. C. Idrobo, M. K. Cinibulk, C. Kisielowski, N. D. Browning, and R. O. Ritchie, Science **306**, 1768 (2004).
[10] N. Nakagawa, H. Y. Hwang, and D. A. Muller, Nature (London) **5**, 204 (2006).
[11] K. Kimoto, T. Asaka, T. Nagai, M. Saito, Y. Matsui, and K. Ishizuka, Nature (London) **450**, 702 (2007).
[12] M. Bosman, V. J. Keast, J. L. Garcia-Munoz, A. J. D'Alfonso, S. D. Findlay, and L. J. Allen, Phys. Rev. Lett. **99**, 086102 (2007).
[13] D. A. Muller, L. F. Kourkoutis, M. Murfitt, J. H. Song, H. Y. Hwang, J. Silcox, N. Dellby, and O. L. Krivanek, Science **319**, 1073 (2008).
[14] T. Mizoguchi, M. Varela, J. P. Buban, T. Yamamoto, and Y. Ikuhara, Phys. Rev. B **77**, 024504 (2008).
[15] G. Yang, Q. Ramasse, and R. F. Klie, Phys. Rev. B **78**, 153109 (2008).
[16] M. T. Anderson, K. B. Greenwood, G. A. Taylor, and K. R. Poeppelmeier, Prog. Solid State Chem. **22**, 197 (1993).
[17] M. T. Anderson and K. R. Poeppelmeier, Chem. Mater. **3**, 476 (1991).
[18] M. Azuma, S. Kaimori, and M. Takano, Chem. Mater. **10**, 3124 (1998).
[19] M. T. Anderson and K. R. Poeppelmeier, J. Solid State Chem. **102**, 164 (1993).
[20] D. L. Novikov, A. J. Freeman, K. R. Poeppelmeier, and V. P. Zhukov, Physica C **252**, 7 (1995).
[21] M. Varela, M. P. Oxley, W. Luo, J. Tao, M. Watanabe, A. R. Lupini, S. T. Pantelides, and S. J. Pennycook, Phys. Rev. B **79**, 085117 (2009).
[22] A. Masuno, M. Haruta, M. Azuma, H. Kurata, S. Isoda, M. Takano, and Y. Shimakawa, Appl. Phys. Lett. **89**, 211913 (2006).
[23] P. Blaha, K. Schwarz, G. K. H. Madsen, D. Kvasnicka, and J. Luitz, *WIEN2k, An Augmented Plane* Wave+Local *Orbitals Program for Calculating Crystal Properties* (Vienna University of Technology, Vienna, Austria, 2002).
[24] C. Hébert, J. Luitz, and P. Schattschneider, Micron **34**, 219 (2003).
[25] R. Egerton, Philos. Mag. **34**, 49 (1976).
[26] J. C. H. Spence, Rep. Prog. Phys. **69**, 725 (2006).
[27] M. Haruta, H. Kurata, H. Komatsu, Y. Shimakawa, and S. Isoda, Ultramicroscopy **109**, 361 (2009).
[28] M. P. Oxley, M. Varela, T. J. Pennycook, K. van Benthem, S. D. Findlay, A. J. D'Alfonso, L. J. Allen, and S. J. Pennycook, Phys. Rev. B **76**, 064303 (2007).
[29] K. Ishizuka, Ultramicroscopy **90**, 71 (2002).

[30] F. A. Cotton, *Chemical Application of Group Theory* (Wiley, New York, 1971).
[31] K. van Benthem, C. Elsässer, and M. Rühle, Ultramicroscopy **96**, 509 (2003).
[32] R. Buczko, G. Duscher, S. J. Pennycook, and S. T. Pantelides, Phys. Rev. Lett. **85**, 2168 (2000).
[33] T. Mizoguchi, I. Tanaka, M. Yoshiya, F. Oba, K. Ogasawara, and H. Adachi, Phys. Rev. B **61**, 2180 (2000).
[34] N. Jiang and J. C. H. Spence, Phys. Rev. B **69**, 115112 (2004).
[35] M. Grioni, M. T. Czyzyk, F. M. F. de Groot, J. C. Fuggle, and B. E. Watts, Phys. Rev. B **39**, 4886 (1989).
[36] F. M. F. de Groot, J. Electron Spectrosc. Relat. Phenom. **67**, 529 (1994).
[37] F. M. F. De Groot, Inorg. Chim. Acta **361**, 850 (2008).